Editors' Suggestion

Scalings and decay of homogeneous, nearly isotropic turbulence behind a jet array

Shiyong Tan, Xu Xu, Yinghe Qi, and Rui Ni*
Department of Mechanical Engineering, The Johns Hopkins University, Baltimore, Maryland 21218, USA

(Received 11 July 2022; accepted 15 December 2022; published 7 February 2023)

Homogeneous and isotropic turbulence can be generated by many different mechanisms, from classical passive grids to jet arrays. By using high-speed jets, a jet array becomes a promising way to produce intense turbulence with large energy dissipation rates in water and wind tunnels. In this paper, a systematic experimental investigation was conducted to understand how the turbulence decay scales with the jet velocity, nozzle size, and nozzle spacings. Three-dimensional particle tracking was performed to quantify the spatial distribution of different turbulent characteristics. Combined with several previous experiments focusing on near-field measurements, our results provide a clear picture of the decay of the kinetic energy and the energy dissipation rate as well as the development of the inhomogeneity and anisotropy of turbulence generated by a jet array. Suggestions and design considerations for future wind and water tunnels are also provided.

DOI: 10.1103/PhysRevFluids.8.024603

I. INTRODUCTION

Turbulent dispersed multiphase flows are ubiquitous in many engineering and environmental applications, such as mineral separation by bubbles in flotation [1], catalytic particles and bubble columns in process technology [2], pollutants dispersed in the atmosphere [3], and plankton in the oceans and sediment-laden river flows [4]. For all these applications, the background flow is turbulent, covering a wide range of temporal and spatial scales. The complex interactions between the dispersed phase and the turbulent carrier phase produce many new phenomena.

To investigate the effect of turbulence, homogeneous and isotropic turbulence (HIT) is commonly used because HIT is a canonical turbulence that retains its universal characteristics without the complications such as the mean shear. Nevertheless, despite the simplicity of HIT, it is nontrivial to produce such an ideal flow in a laboratory setting in a controlled way. HIT can only be approximately generated in the laboratory because it is challenging to produce turbulent energy across the entire flow domain uniformly. The most common and successful way of generating HIT is by adding a periodic grid or mesh in wind or water tunnels, which was first attempted by Simmons and Salter [5]. In these systems, flows were shown to be homogeneous in two-dimensional (2D) planes parallel to the grid [6,7] with the spatial decay of turbulent kinetic energy (TKE) in the third direction. To reach a state of satisfactory isotropy, the individual wakes induced by a "passive" grid require at least 30 mesh lengths to fully mix and merge with each other [8]. At such a distance, turbulence has weakened, resulting in a moderate Taylor-Reynolds number [9–11], $\mathrm{Re}_\lambda = u'\lambda/\nu$ between 50 and 150 [u' is the root-mean-squared (rms) fluctuation velocity, λ is the Taylor microscale $\lambda = \sqrt{15\nu/\epsilon}u'$, ϵ is the turbulent energy dissipation rate, and ν is the kinematic viscosity of the fluid]. In attempts to increase the Re_λ, "active" grids with randomly flapped agitator wings [12] replaced the passive predecessors, and it can significantly enhance Re_λ [13–16].

*rui.ni@jhu.edu

However, both turbulence and its Reynolds number will not be kept constant in wind or water tunnels driven by a grid; they continue to decay as turbulence moves away from the grid. Such decay is controlled directly by the energy dissipation rate $\epsilon = 2\nu\langle S_{ij}S_{ij}\rangle$ (ν is the kinematic viscosity and S_{ij} represents the rate-of-strain tensor). If the turbulence attained is homogeneous and isotropic and Taylor's frozen flow hypothesis is used, the decay of the kinetic energy as a function of distance away from the grid can be converted to the decay in time, which follows a power-law relationship $k = u'^2/2 \sim t^{-n}$; the same applies to the growth of the integral length scale $L \sim t^m$ [17,18]. At high enough Reynolds numbers, the exponent n is believed to be a universal constant [9,19,20]. Invoking self-similarity, it was shown by Batchelor [9] that $n = 1$ and $m = 1/2$. Assuming invariants related to the energy spectrum near small wave number, different power-law exponents were derived before, which shows $n = 6/5$ and $m = 2/5$ by Birkhoff [19] and Saffman [20]. Furthermore, assuming the growth of the length scale is limited by the size of the turbulence box $L \sim t^0$ and the decay is driven by the mean energy dissipation rate $\langle\epsilon\rangle$, one can also acquire $n = 2$ and $m = 0$ [21–23].

Such a wide spread of the exponent for the decaying turbulence was also reported in experiments by using conventional grids [10,24], fractal grids [7,25–28], rotating grid rods [29], as well as active grids [11,12]. The reported exponent n ranges from 1 to 2 with the majority of experiments using conventional grids consistent with Birkhoff-Saffman prediction of $n = 6/5$.

In addition to grids (active or passive), turbulence can also be generated by jets. An important work that should be noted is by Gad-el Hak and Corrsin [8], in which an array of nozzles were integrated with a conventional passive grid. Jets from these nozzles can be independently controlled and, depending on the injection rate from the nozzle, a systematical change of the decay power-law exponent from $n = 1.325$ to 1.0 as the jet-injection rate increases was observed. This finding is counterintuitive because jets are shown to improve the energy transfer in the high-wave-number regions, which is expected to increase instead of decrease the decay rate. This inconsistency calls for more studies to understand turbulence decay driven by a jet array.

Note that, in this previous work, the jet array was used primarily to assist the passive grid to generate turbulence. The flow rate through the jets was only 8.55% of the co-flow. In a more recent work by Variano and Cowen [30], the jet array was employed to drive turbulence without a co-flow, and the results suggested a much larger exponent of $n = 2$, which seems to imply that increasing the jet flow rate tends to first reduce and then increase the decay exponent. A similar exponent ranging from $n = 1.89$ to 2.13 can also be extracted from the measured decay of the turbulent kinetic energy for different jet actuation patterns by Pérez-Alvarado, Mydlarski, and Gaskin [31]. A slightly lower exponent close to 1.65 can be roughly estimated from Fig. 6 reported by Johnson and Cowen [32]. Note that, in this case, the turbulence generated was confined in a box so the decay could be affected.

To cover the range of the jet flow rates between these two limits, the goal in this paper is to understand the turbulence decay driven by a jet array with the jet flow rate ranging from 18.5% to 87.2% of the total flow rates. In particular, the paper focuses on how different turbulent characteristics scale with the jet nozzle diameter and jet velocity. The detail of the experiments is introduced in Sec. II. In Sec. III, we first derive the location where HIT starts to form based on previous experiments and present the results on the decay of fluctuation velocity and the dissipation rate. Based on the measurements, a simple empirical equation is proposed to quantify the decay. Finally, some practical design considerations are shared for future experimental studies.

II. EXPERIMENTAL SETUP

All the experiments were performed in a closed-loop vertical water tunnel, called a vertical octagonal noncorrosive stirred energetic turbulence (V-ONSET), as shown in Fig. 1. In this tunnel, turbulence was powered by a three-dimensional (3D) printed jet array facing downward at the top of a transparent octagonal test section (for details, see Masuk *et al.* [33]).

For the jet array, there are four important parameters, including the number N of nozzles, the nozzle size d, the nozzle spacing M, the co-flow velocity U_c, and the jet velocity V_{jet} at the nozzle

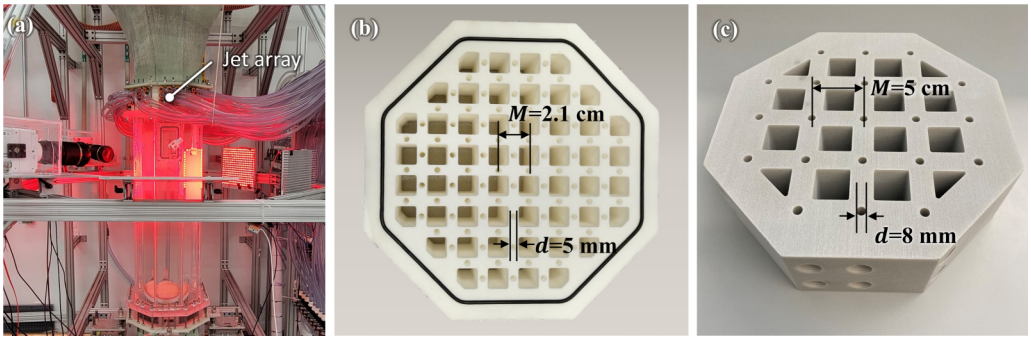

FIG. 1. Pictures of (a) the V-ONSET with an optical diagnostic system and (b), (c) two different jet arrays: (b) Array 1 and (c) Array 2.

exit. Note that, for a given jet array, the jet spacing is fixed, but M can vary by turning on more or fewer jets in experiments. As shown in Fig. 1, two different arrays were printed: (Array 1) $N = 88$, $d = 5$ mm, $M = 2.1$ cm, (Array 2) $N = 21$, $d = 8$ mm, $M = 5$ cm. Here, the values of M are referred to the case when all the jets are on.

As shown in Fig. 2(a), each nozzle was connected through internal channels to their individual side openings, which can be controlled separately by solenoid valves. Although jets can be turned on and off randomly in space and time, the experiments reported in this work were conducted by keeping the designated jets running continuously in order to keep a constant spacing between neighboring jets. In addition, squared through holes between these nozzles allow co-flow to merge coaxially with the firing jets. To drive the flow, a single centrifugal pump with a variable frequency controller was used. The split of the flow coming out of the pump between the co-flow and jet array can be controlled by a regulating valve. This method allows for independent control of the co-flow U_c and the jet exit velocity V_{jet}, which were precisely measured by two flow meters installed in the system.

To measure turbulence and acquire its statistics, three high-speed cameras were used to capture the tracer motion inside the tunnel. The shadows of the seeded polyamide tracer particles with 60 μm in diameter and density close to 1.03 g/cm^3 were cast by a dedicated LED panel onto the imaging plane of each camera. These images were then reconstructed into 3D trajectories via our in-house open-source Lagrangian particle tracking algorithm, OpenLPT [34,35]. The entire optical diagnostic system was mounted on a frame that can be slid to different positions away from the jet array.

To investigate turbulence decay driven by a jet array, we conducted experiments by changing V_{jet}, M, and the measurement location x from the jet array. Each experimental condition was repeated to cover at least four times the integral timescale T_L. The view volume is around 6 cm in width and 3 cm in height, which covers at least one integral length scale L to ensure that the inertial range statistics are fully resolved. For all the data presented, V_{jet} was varied between 2.4 to 12.1 m/s; the jet spacing ranges from $M = 2.8$ to 5.4 cm. The jet spacing was controlled by changing the number of jets that are on since individual nozzles can be independently controlled by the solenoid valves. The statistics were acquired up to 100 times the nozzle diameter away from the jet array. Details of the experimental conditions are summarized in Table I.

III. RESULTS

A. Homogeneity

Previous works have shown that a jet array can produce turbulence close to a homogeneous and isotropic condition [8,30,33,36–38]. However, in most cases, the measurements were limited to

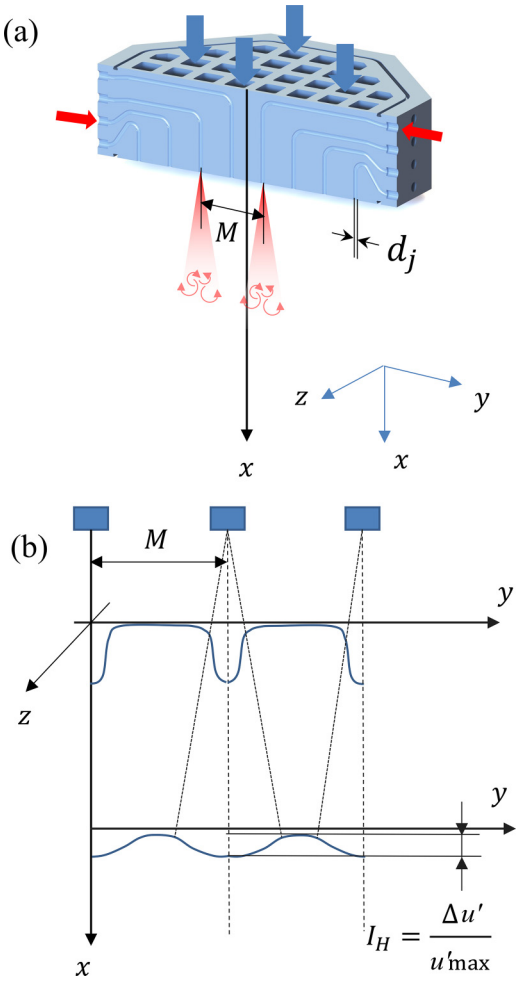

FIG. 2. (a) Section view of a jet array to show the internal channels and key geometric parameters; (b) Schematic of the mean velocity profile at two different axial locations.

TABLE I. Control parameters for experiments.

Experiment	Array	V_{jet} (m/s)	U_c (m/s)	M (cm)	x/d
I.1	Array 1	5.5	0.27	2.8	[53,165]
I.2	Array 1	5.5	0.27	3.2	[53,165]
I.3	Array 1	5.5	0.27	4.0	[53,165]
I.4	Array 1	5.5	0.27	5.4	[53,165]
II.1	Array 1	2.5	0.22	5.9	76
II.2	Array 1	5.33	0.22	5.9	76
II.3	Array 1	5.46	0.22	5.9	76
II.4	Array 1	7.2	0.22	5.9	76
II.5	Array 1	7.75	0.22	5.9	76
II.6	Array 1	10.3	0.22	5.9	76
II.7	Array 1	11.8	0.22	5.9	76
II.8	Array 1	12.1	0.22	5.9	76
III	Array 2	7	0	6.9	37.5

regions that are sufficiently far from the jet array. Since turbulence continues to decay as it moves away from the jet array, for studies that aim at reaching intense turbulence, it is beneficial to stay close to the jet array. It is therefore important to know the minimum distance away from the jet array so that one can assume homogeneity and isotropy.

Although such near-field data are not available from the turbulence community, many experiments and simulations were conducted before to understand interacting jets, including those aligned in a row [39], an array [40–44], or just between two [45–48]. These studies focused exclusively on the near-field jet dynamics so they provided a detailed description of the flow velocity profile, jet interaction, and the decay of the centerline velocity.

Figure 2(b) shows the mean flow profile developed in the near field of a jet array. In this case, three boxes represent the three nozzle exits. Close to the array, the signature of each individual jet is visible; as the flow continues to move downstream, the jets start to merge. To fully capture this evolution, a dataset from Ghahremanian *et al.* [44] is used. In this work, the jet array was not connected to a water tunnel but exposed to a large ambient environment. As a result, jets near the edges were affected by the pressure gradient so only the velocity profiles from the two center jets are used. The time-averaged axial velocity $\langle V_i \rangle$ normalized by V_{jet} is shown in Fig. 3 as a function of the transverse direction (y axis) normalized by the jet diameter d. Different colors represent the velocity profiles at different axial locations away from the nozzle exits, and it is evident that the mean flow is almost uniform along the transverse direction at around $5.5M$ away from the jet array.

For a single statistically axisymmetric, stationary nonswirling jet, the problem can be solved by using the boundary-layer momentum equation [50] with the Reynolds stress modeled by the eddy viscosity method. However, the problem becomes much more complicated when multiple jets are considered. Since such a solution is not readily available, we can simplify the problem by assuming that, in the near field close to the jet array, individual jets still follow the self-similar velocity profile, which can be expressed as

$$f(\eta) = \frac{\langle V_1(x, y) \rangle}{V_c(x)} = \frac{1}{(1 + a\eta^2)^2}, \tag{1}$$

where the mean axial jet velocity $\langle V_1(x, y) \rangle$ normalized by the jet centerline velocity $V_c(x)$ is a function of $\eta = y/(x - x_0)$ (x_0 is the virtual origin). The coefficient $a = (\sqrt{2} - 1)/S^2$ is related to the spreading rate $S = 0.094$ in a single jet [50]. The centerline velocity $V_c(x)$ at a particular axial location follows

$$\frac{V_c(x)}{V_{\text{jet}}} = \frac{Bd}{(x - x_0)}, \tag{2}$$

where B is an empirical constant that depends only on the jet configuration, e.g., whether the jet is surrounded by a nonzero co-flow in the background.

As shown in Fig. 2, the simplest way to estimate the mean velocity profile is by assuming a linear superposition of the individual jet profile between two adjacent jets located at $y_1 = 0$ and $y_2 = M$ with a spacing of M, which yields

$$\frac{\langle V_1(x, y) \rangle}{V_c(x)} = \frac{1}{[1 + a(y/x)^2]^2} + \frac{1}{\{1 + a[(y - M)/x]^2\}^2}. \tag{3}$$

The results are shown as solid lines in Fig. 3(a), which are in good agreement with the experiment data and implies that the estimation based on the linear superposition works well for predicting the mean flow profile produced by a jet array. In particular, at around $x/M = 5.5$, the profile is close to being flat, indicating that the mean flow is uniform along the lateral direction.

Apart from the mean flow, the homogeneity of turbulence has to be quantified by the fluctuation velocity $v_i = V_i - \langle V_i \rangle$ ($i = 1, 2, 3$ for three directions), particularly the variance of its axial component, i.e., $v_1' = \langle v_1^2 \rangle^{1/2}$. From the same experiment, the profile of v_1' downstream of a jet array is also available, which is shown in Fig. 3(b) at three different axial locations. It is evident that the flow inhomogeneity decays with x. Close to $x/M = 5.5$, the profile of v_1' is almost flat. To predict where

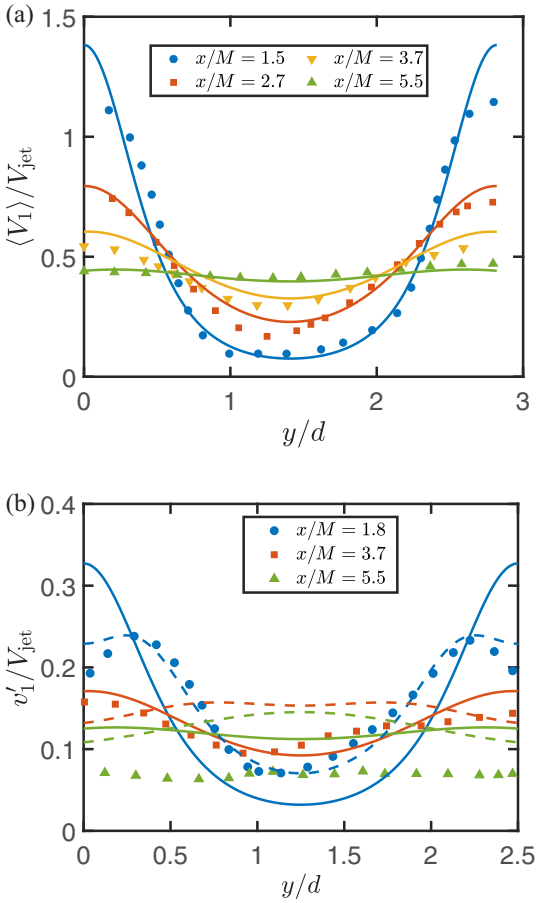

FIG. 3. The profile of (a) the mean and (b) the fluctuation velocity for two adjacent jets, located at $y = 0$ and $y = 2.9d$, in a jet array along the transverse direction y. In both figures, the symbols represent the experimental measurements [44] at different downstream locations. The solid lines in panel (a) are obtained from Eq. (3), and those in panel (b) are calculated by multiplying the mean velocity with a coefficient $C_0 = 0.28$. The dashed lines in panel (b) show the results of superposing the velocity fluctuations of two single jets based on the measurements by Hussein, Capp, and George [49].

the homogeneous condition is reached, the linear superposition, but using the profile of v_1' from a single jet obtained from a previous work [49], is attempted [see dashed lines in Fig. 3(b)]. Although the data agree well with the superposed result at $x/M = 1.8$, the difference grows as x increases. In particular, for $x/M > 1.8$, the superposed results indicate that the peak of v_1' is not located at the centerline as the data suggest, but about $0.3d$ away from each nozzle. This deviation clearly shows the limitation of this method.

The alternative way to estimate the fluctuation velocity profile is via the mean velocity profile. For a single jet, the ratio between v_1' and $\langle V_1 \rangle$ is consistent at different x locations. The fluctuation velocity profile for the jet array can therefore be estimated by multiplying $\langle V_1 \rangle$ [Eq. (3)] with a coefficient of $C_0 = 0.28$. Such a coefficient should vary in a large range and depend on the radial direction away from the jet centerline. Nevertheless, for simplicity, it is assumed to be a constant, independent of the y axis. This assumption should only overestimate the inhomogeneity of the turbulence because $v_1'/\langle V_1 \rangle$ grows as it moves away from the jet centerline, which will only serve to smooth the profile of v_1'. The prediction is plotted in Fig. 3(b) as the solid lines. This estimation

cannot capture the profile at $x/M = 1.8$ as expected because, unlike v_1 that peaks at the jet edges due to the growing shear layer, the mean flow does not. But as it moves downstream and flow becomes fully developed, e.g., $x/M = 3.7$ and $x/M = 5.5$, the prediction based on the mean flow works much better, capturing the evolution of the velocity profile. The only problem with this method is that it overestimates the overall magnitude of the fluctuation velocity because C_0 was assumed to be a constant. But this deviation does not affect the estimation of the flow inhomogeneity.

To quantitatively define the inhomogeneity level, the maximum and minimum fluctuation velocity between two adjacent jets can be expressed as

$$\frac{v'_{1,\max}(x)}{V_c(x)} = C_0 + \frac{C_0}{(1 + aM^2/x^2)^2}, \quad \frac{v'_{1,\min}(x)}{V_c(x)} = \frac{2C_0}{[1 + a(M/2x)^2]^2}. \tag{4}$$

From these two fluctuation velocities, the turbulence inhomogeneity factor can be defined as $I_H(x) = (v'_{1,\max} - v'_{1,\min})/v'_{1,\max} = 1 - v'_{1,\min}/v'_{1,\max}$, which varies between 0 and 1 and can be expressed explicitly as a function of x:

$$I_H(x) = 1 - \frac{2(1 + aM^2/x^2)^2}{(1 + aM^2/4x^2)^2[(1 + aM^2/x^2)^2 + 1]}. \tag{5}$$

$I_H = 0.1$ is set as the threshold for inhomogeneity, and flows with I_H lower this threshold can be assumed to be homogeneous. This model clearly suggests that the flow reaches the homogeneous condition for $x > 5.5M$, matching exactly to what was acquired from the experimental results.

This solution suggests that the minimum distance away from an array of jets to reach fully homogeneous turbulence is around six times the jet spacing and is independent of the jet velocity V_{jet} and the nozzle diameter d as long as d is small enough ($d \ll x$) to meet the condition for the self-similar jet velocity profile expressed in Eq. (1). This conclusion is consistent with a previous work [36], which suggested that the flow becomes homogeneous at $6M$.

Note that the condition discussed here assumes a weak co-flow, and the turbulence is driven solely by the jet momentum. The other limit can be reached if the co-flow is as strong as the jet, in which case turbulence will not be generated. Between these two limits, we anticipate that adding co-flow will result in weaker turbulence, lower spreading rate [51], and possibly a longer distance before the homogeneity condition can be reached. The exact number can be roughly estimated based on Eq. (1) by updating the spreading rate S used in a.

B. Turbulence in V-ONSET

In the previous section, we focused on the profile of the jet velocity, including $\langle V_i \rangle$ and v_i, as two neighboring jets mix. In this section, we shift our attention to the fully developed turbulence generated by a jet array. In particular, the statistics was taken at $x = 5.7M$ away from a jet array (Array 1) with the jet spacing of $M = 5.4$ cm in V-ONSET (Experiment I.4 in Table I). According to the prediction in Sec. III A, turbulence at this location should be homogeneous. To distinguish the turbulence statistics in this system from the discussion of jets, the mean velocity and the variance of the fluctuation velocity in the test section are denoted as $\langle U_i \rangle$ and u_i ($i = 1, 2, 3$ represents three directions), respectively.

Figure 4 shows the probability density function (PDF) of u_i in three directions plotted against the standard normal distribution. As seen in Fig. 4, all components of velocity fluctuation are nearly identical and match the Gaussian distribution. Figures 5(a) and 5(b) show the spatial variation of both $\langle U_i \rangle$ and u'_i along the x and y axes, respectively, where u'_i is the mean-square fluctuation. In Fig. 5, each data point is shown with error bars indicating the 95% confidence intervals (CIs) of the estimations. But the error bar is too small to discern from the markers because of the large number of tracer trajectories acquired in each experiment. As seen in both Figs. 5(a) and 5(b), the profile for all velocities, including both the mean and the fluctuation components, remains almost constant along both the axial and transverse directions, suggesting that the flow is nearly homogeneous.

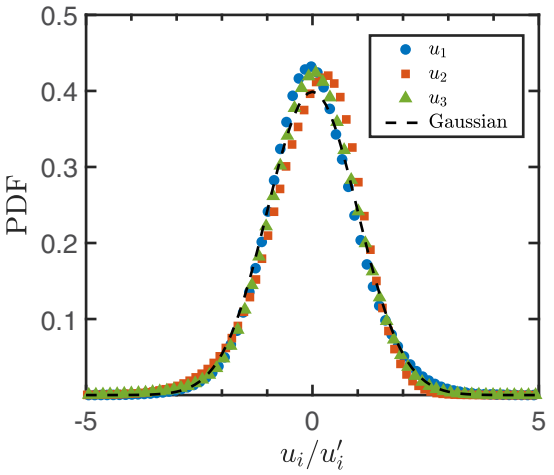

FIG. 4. The PDF of the fluctuation velocity normalized by their standard deviation from Experiment I.4 at $x = 5.7M$. The dashed line indicates the standard normal distribution.

From the data shown in Fig. 5, one can also calculate the ratio $u_2'/u_3' \approx 0.9887$, with 95% CI of [0.9874 0.9898], and $u_1'/u_2' \approx 1.163$, with 95% CI of [1.160 1.167], both of which are close to 1, indicating that the turbulence is also nearly isotropic, although the vertical component is slightly larger than the horizontal components since it gains the energy directly from the jet flow.

Another way to investigate the isotropy of turbulence is by using the Reynolds stress tensor $\tau_{ij} = \langle u_i u_j \rangle$, which can be decomposed into the isotropic ($i = j$) and anisotropic part ($i \neq j$). The anisotropic part should be zero in isotropic turbulence. One component, normalized by the TKE, $k = \langle u_i u_i \rangle/2$, is shown in Fig. 6, which covers a range of x/d from 5.0 to 51.8. Two dashed lines represent $\pm 10\%$ about zero. Close to the nozzle, the Reynolds stress shows a significant variation, and such a variation decays rapidly. To ensure all the anisotropic components of τ_{ij} are close to zero in all directions in the far field, Fig. 7 shows the remaining components along all three directions at $x/d = 61.6$ using Array 1. It is evident that all symbols are well within the two dashed lines, suggesting that the flow is nearly isotropic.

The decay of the anisotropic component of τ_{ij} along the x axis can be more quantitatively shown by taking the spatial standard deviation along the y direction, i.e., $\xi_{ij}(x) = [\langle \tau_{ij}^2(x, y) \rangle]_y^{1/2}$, for each x position. The results obtained from the experiments using Array 1 at different jet spacings are shown in Fig. 8. The measured Reynolds stress is plotted against x/d instead of x/M because the data only collapse when x is normalized by the nozzle diameter. Consistent with Fig. 6, the variation of τ_{ij} decays continuously as a function of x/d. And it falls below 10% at around $x = 20d$.

As a result, the criteria for reaching homogeneous versus isotropic conditions are not the same. The homogeneous condition relies more on the mixing between neighboring jets with a spacing of M, while the isotropic condition is driven primarily by the turbulence transported from the shear layer within the individual jets along the x axis to the other two directions. The two criteria ($x > 6M$ and $x > 20$d) may not coincide for a given jet configuration, and the axial location should be selected to meet both requirements for reaching nearly homogeneous and isotropic turbulence.

C. Turbulence decay

After reaching nearly homogeneous and isotropic conditions, turbulence continues to decay as it moves away from the jet array. To investigate the turbulence decay along the axial direction, $u' \equiv (u_1'^2 + u_2'^2 + u_3'^2)^{1/2}$ was measured at multiple x away from the jet array, as described in Sec. II. In addition to our datasets, the near-field measurements [44] at two smaller x locations along with

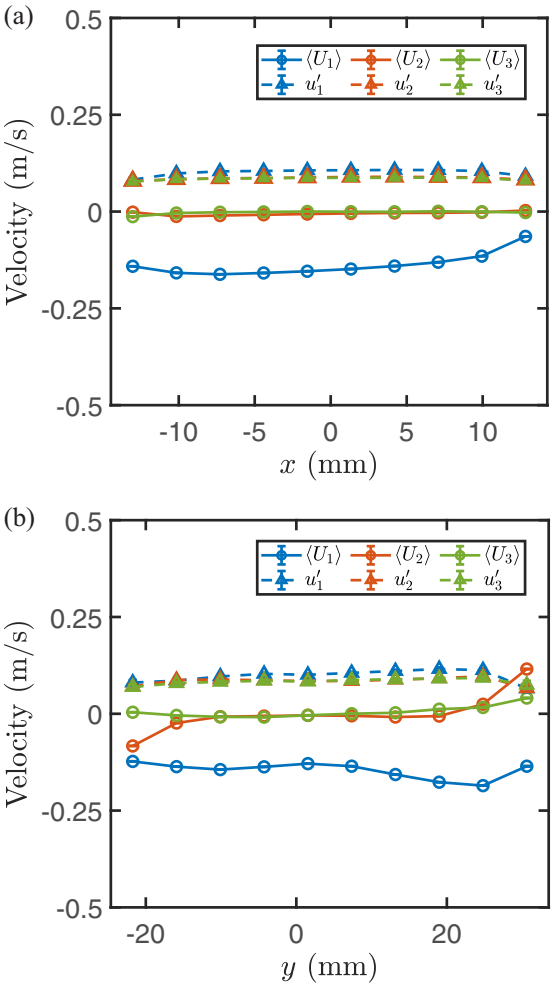

FIG. 5. The profile of both the mean and fluctuation velocities along the axial and transverse directions from Experiment I.4 at $x = 5.7M$.

a result from another jet array experiment [36] are also included. Together, the data covers over a decade of the axial distance for understanding the decay of turbulence produced by a jet array.

u'/V_{jet} is plotted against x normalized by the jet diameter d or by the jet spacing M (inset) in Fig. 9. It is evident that the only way to collapse all the datasets is by using the jet diameter as the characteristic length scale, not the jet spacing M, even though M was used to determine where the homogeneous condition is reached. Therefore, the roles played by these two length scales are different: M controls the lateral mixing to determine where the jet is fully mixed with each other, but turbulence is driven by the shear layer instability from individual nozzles. The nozzle diameter imprints on the statistics much further downstream even after the neighboring jets are fully mixed.

The compiled data suggests that u' seems to scale with x^{-1}, which is consistent with the finding by Variano and Cowen [30]. But the scaling exponent of the decaying kinetic energy $n = 2$ is larger than those reported by most experiments studying decaying-turbulence [7,10–12,24–29] and also by an earlier work conducted in the Johns Hopkins University Stanley Corrsin wind tunnel [8]. In this wind tunnel, jets were integrated with the classical passive grid, and n is found to range between 1 and 1.325.

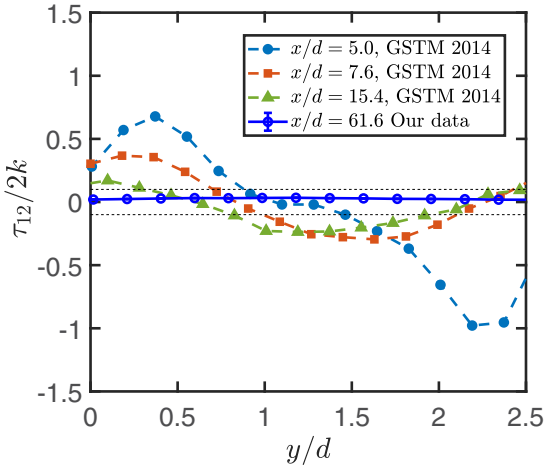

FIG. 6. One component of the Reynolds stress at four different axial locations downstream of a jet array. The three near-field measurements ($x/d \leqslant 15$) were from the work by Ghahremanian *et al.* [44] (GSTM 2014) and the remaining far-field result ($x/d \gg 15$) was acquired from Experiment I.4 using Array 1 at $x = 5.7M$.

An important distinction between the two setups needs to be drawn. In our experiments, the goal is to increase turbulence in a configuration with a relatively weak co-flow. The injection rate J, defined as the ratio between the mass flow rate by the jets to the co-flow, ranges from 18.5% to 87.2%. For the wind tunnel experiments [8], the momentum of jets was maintained to be below 10% of that of the co-flow, the turbulence production method is still dominated by the co-flow passing through a grid.

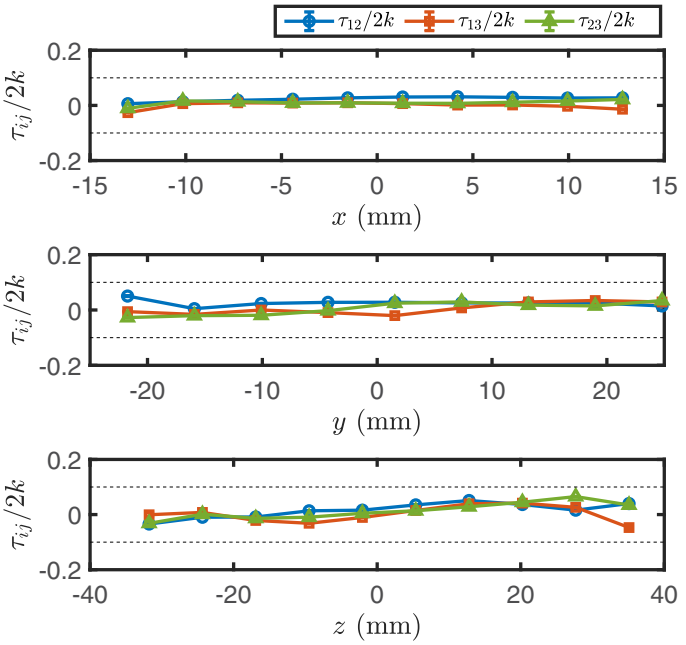

FIG. 7. The spatial profile of the three components of the Reynolds stress tensor normalized by the local TKE from Experiment I.4 at $x = 5.7M$. The dashed lines show the 10% variation.

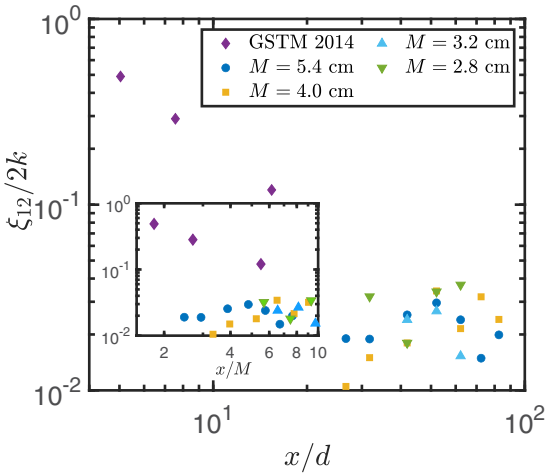

FIG. 8. The decay of the spatial variation of the Reynolds stress as a function of the normalized axial location. Purple diamonds represent the near-field data from the work by Ghahremanian *et al.* [44] (GSTM 2014), and other markers represent our data from Experiment I.1–I.4 using different jet spacings M.

Furthermore, Gad-el Hak and Corrsin [8] found out that n decreases from 1.325 to 1 as J increases from 4.7% to 8%, which implies that stronger jets yield slower turbulence decay. This finding was originally hypothesized to be linked to the possible more energy in small wave numbers in power spectra. But the authors realize later in their paper that this hypothesis is opposite to their measured results, in which the jets actually introduced more energy in high wave numbers. This inconsistency led to the conclusion that the jets may have dynamic interaction with the turbulent wake after the passive grid that changes the decaying rate.

One way to model the decay of u' driven by a jet array is to assume that the memory of the jet configuration survives far downstream, and the decay follows a similar way as that for a single jet. Following the same argument about the relationship between the mean and the fluctuation, the

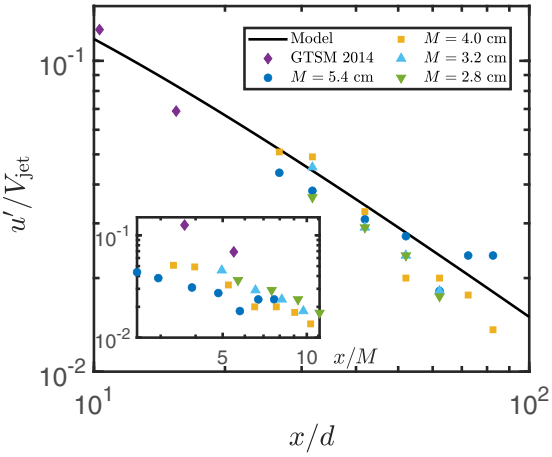

FIG. 9. The decay of turbulent velocity fluctuations as a function of the axial location normalized by d or M (inset). Data presented in this figure are the same as those described in Fig. 8. The black solid line is obtained from Eq. (6).

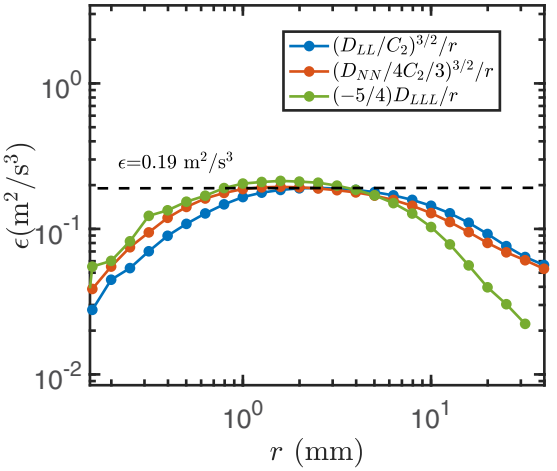

FIG. 10. The compensated velocity structure functions versus the separation between the two velocity vectors from Experiment I.4 at $x = 2.9M$.

decay of u' can be modeled based on Eq. (2) following,

$$\frac{u'(x)}{V_{\text{jet}}} = \frac{C_0 B d}{x}, \tag{6}$$

where the virtual origin x_0 is neglected for the far-field statistics. The parameter B will be discussed later. The result is shown in Fig. 9 as the solid line, which agrees well with not only our data but the previous near-field measurements [44]. This finding confirms our conjecture that the decay of turbulence driven by a jet array shares similarities with that driven by a single jet even at a distance far away from the array, where the neighboring jets have already fully merged.

D. Decay of turbulent energy dissipation rate

The key advantage of employing a jet array, instead of a grid (passive or active), to drive turbulence is the large range of turbulence characteristics that can be acquired with a simple control system. Other than the fluctuation velocity that pertains to the large-scale flows, the small-scale dynamics is determined by the energy dissipation rate ϵ, which is another key quantity of interest. In our study, ϵ is estimated from the calculation of the second-order velocity structure function $D_{ij}(r) = \langle u_i(\mathbf{x})u_j(\mathbf{x}+\mathbf{r})\rangle$, where $\mathbf{x}$ and $\mathbf{r}$ are the position of fluid particles and the separation between a pair. Based on the well-known Kolmogorov theory [52], it is known that $D_{LL} = C_2(\epsilon r)^{2/3}$ and $D_{NN} = 4C_2(\epsilon r)^{2/3}/3$, where D_{LL} and D_{NN} are the longitudinal and transverse components of $D_{ij}(r)$ respectively. The Kolmogorov constant C_2, although depending on Re_λ [53], can be assumed to be about 2.1. In addition, the third-order structure function in the inertial range follows $D_{LLL} = -4\epsilon r/5$. Figure 10 shows a plot of the three structure functions compensated by their respective scaling laws from Experiment I.4 at $x = 15.9$ cm downstream. The plateau, albeit narrow, in Fig. 10 suggests that $\epsilon \approx 0.19$ m^2/s^3.

To establish the relationship between ϵ with the axial position x away from the jet array, we can leverage a well-known relation, $\epsilon \approx C_\epsilon u'^3/L$ where C_ϵ is an order-unity constant [54], i.e., $C_\epsilon \approx 0.73$ for $Re_\lambda > 100$. For decaying isotropic turbulence, the integral scale follows $L \sim x^{-1/2}$ based on the work by George [55]. To confirm this scaling, in Fig. 11, the measured dissipation rate is shown as a function of $u'^3/x^{1/2}$, and the solid line indicates a linear relationship. If L does scale with $x^{-1/2}$, the data should agree with the solid line. The evident overall agreement between the two

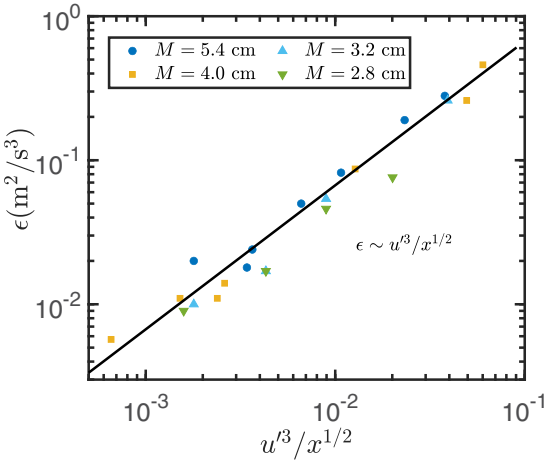

FIG. 11. The correlation between the turbulent energy dissipation rate ϵ and $u'^3/x^{1/2}$ for all the datasets collected from Experiment I.1–I.4.

in the figure indeed confirms that the growth of the integral scale in decaying turbulence driven by a jet array is similar to those driven by a passive grid.

In addition, since the data containing different jet spacings M collapse together, it implies that ϵ may be insensitive to M, and the nozzle diameter is the only length scale that matters to ϵ. So the integral scale $L(x)$ can be expressed as

$$L(x) = K(dx)^{1/2}, \tag{7}$$

where K is a coefficient that can be obtained by fitting Eq. (7) with the experimental data shown in Fig. 11, yielding $K \approx 3.31$.

By using Eqs. (6) and (7), we arrive at the equation for ϵ as follows:

$$\frac{\epsilon}{V_{\mathrm{jet}}^3/d} = \frac{C_\epsilon C_0^3 B^3}{K(x/d)^{7/2}}. \tag{8}$$

This formulation suggests that the energy dissipation rate is only a function of the jet velocity and the jet diameter, independent of the jet spacing.

Figure 12 shows the normalized energy dissipation rate at different normalized axial locations for Array 1. In addition, the solid line shows the model prediction. The only parameter that has not been discussed before in the model is B, which comes from Eq. (2). B depends on whether the jet is surrounded by a co-flow. Its value has been independently obtained before in a different experiment that systematically studied the jet profile with and without a co-flow [56]. Based on the velocity ratio for all the experiments with Array 1, the velocity ratio is close to 20.4, with $V_{\mathrm{jet}} = 5.5$ m/s and the co-flow velocity near the nozzle being 0.27 m/s. For the closest velocity ratio $R = 20$ reported by Or, Lam, and Liu [56], the parameter B is roughly 5.47, which is used for plotting the solid line in Fig. 12. Despite the scatter in the data, it seems to agree with our data within the measurement uncertainty.

In addition to Array 1, Array 2 was tested without a co-flow, and the turbulent energy dissipation rate generated is found to be larger than the data taken using Array 1. Furthermore, the result from Variano and Cowen [30] using $d = 21.9$ mm and $V_{\mathrm{jet}} = 0.6$ m/s without a co-flow is also added, which also seems to be larger. To account for this difference, the parameter B in Eq. (8) is modified by using the value from the work by Hussein, Capp, and George [49], i.e., $B = 5.8$. The prediction is shown as the dashed line, which agrees perfectly with the two datasets mentioned before in a configuration without a co-flow.

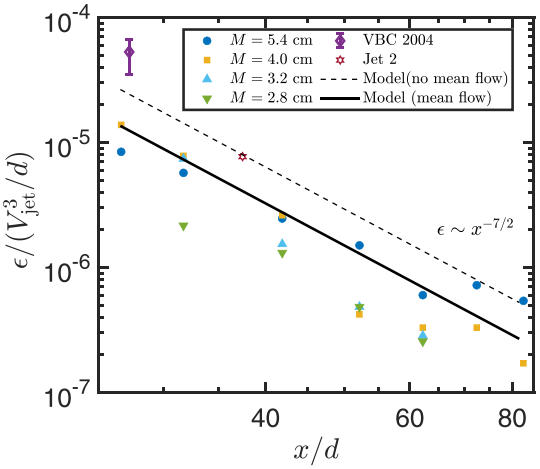

FIG. 12. The decay of the normalized energy dissipation rate versus the normalized axial location. The purple diamond represents the data from experiments by Variano, Bodenschatz, and Cowen [36] (VBC 2004). The brown hexagram is acquired from Experiment III and other markers from Experiment I.1–I.4. The black solid and dash lines are obtained from Eq. (8).

E. Design suggestions

From a practical standpoint, Eqs. (2), (7), and (8) provide a way to estimate u', L, ϵ in a water tunnel driven by a jet array, by controlling the jet velocity, nozzle size, and jet spacing. Although these equations are simple to use, there are several important design considerations that need to be discussed for future experiments. First of all, in Eq. (8), it is shown that ϵ scales with $V_{\rm jet}^3$. Most datasets reported in previous figures used the same jet velocity. To confirm the scaling of the energy dissipation with the jet velocity, experiments were conducted to measure ϵ at a constant $x/d = 76$ away from the jet array (Array 1) for different jet velocities, the results of which are shown in Fig. 13. The jet velocity spans almost a decade and it is clear that the data follows the cubic scaling, i.e., $\epsilon \propto V_{\rm jet}^3$.

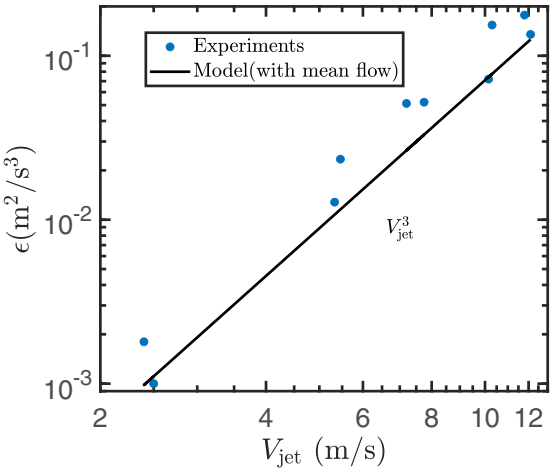

FIG. 13. The turbulence energy dissipation rate as a function of the jet velocity collected from Experiment II.1–II.8. The black solid line is obtained by Eq. (8).

The jet velocity here was varied by using the variable frequency controller of the pump. The maximum jet velocity is determined both by the pump capacity as well as the nozzle size and number. To further increase ϵ, one may attempt reducing the nozzle size; with the same flow rate, V_{jet} can be increased further. This only works if x/d is maintained the same, which means the measurement window needs to move closer to the jet array with a small nozzle size. The price that one has to pay is to have more jets and smaller spacing M to ensure the flow is homogeneous and isotropic.

Another key aspect is related to the pump and the piping systems that drive the jet array. Each jet needs to be connected to the pressure vessel through at least one solenoid valve. A pressure manifold is also needed to distribute an even pressure head to all jets. All these systems will add to the pressure drop of the system. It is important to select the nozzle and pipe size to balance the flow rate and pressure drop of the system so the pump operates at its highest efficiency. Deviating from this point too much could result in pump cavitation and other undesired effects.

IV. CONCLUSION

We have shown the decay of turbulence powered by a jet array in a vertical water tunnel. Two arrays with different nozzle sizes and spacings were printed to systematically investigate how different turbulent characteristics scale with the control parameters. In addition to the experimental results, a simple model relying on the superposition of two jets was designed to explain the flow development. It is found that, for the multijet flow to develop into homogeneous turbulence, a distance of at least 5.5 times the jet spacing downstream from the array is required. The isotropy condition can be met at around 20 times the nozzle diameter, which was examined both by the velocity profile along different directions and also by whether the Reynolds stress is close to zero.

After homogeneous and isotropic turbulence is reached, turbulence continues to decay downstream with the magnitude of rms velocity decreasing as x^{-1}. Such decay is mainly determined by the nozzle diameter and insensitive to the jet spacing M because turbulence is driven by the shear layer instability originating from individual nozzles. Furthermore, the decay exponent of the kinetic energy is roughly $n = 2$, which is higher than those reported by most experiments using a classical passive grid. This higher exponent is attributed to the memory of the jet, which is different from the one caused by the wake after a grid.

Based on the evolution of the velocity fluctuation and the integral length scale downstream, a formulation of the energy dissipation rate ϵ is derived, which matches well with not only our experimental data with a co-flow but also with a previous work without a co-flow. Finally, design considerations were provided to help future wind or water tunnels use this method to drive turbulence, which can potentially reach much more intense turbulence with a higher energy dissipation rate than that produced by classical passive or active grids.

ACKNOWLEDGMENTS

We acknowledge the financial support from the National Science Foundation under the Award No. CAREER-1905103. This project was also partially supported by the ONR award: N00014-21-1-2083.

[1] H. Schubert, On the turbulence-controlled microprocesses in flotation machines, Int. J. Miner. Process. **56**, 257 (1999).

[2] M. Pourtousi, J. Sahu, and P. Ganesan, Effect of interfacial forces and turbulence models on predicting flow pattern inside the bubble column, Chem. Eng. Process. **75**, 38 (2014).

[3] Á. Leelőssy, F. Molnár, F. Izsák, Á. Havasi, I. Lagzi, and R. Mészáros, Dispersion modeling of air pollutants in the atmosphere: a review, Open Geosci. **6**, 257 (2014).

[4] F. Peters and C. Marrasé, Effects of turbulence on plankton: An overview of experimental evidence and some theoretical considerations, Mar. Ecol. Prog. Ser. **205**, 291 (2000).
[5] L. F. G. Simmons and C. Salter, Experimental investigation and analysis of the velocity variations in turbulent flow, Proc. R. Soc. Lond., Contain. Pap. Math. Phys. Character **145**, 212 (1934).
[6] T. Kurian and J. H. Fransson, Grid-generated turbulence revisited, Fluid Dyn. Res. **41**, 021403 (2009).
[7] P.-Å. Krogstad and P. Davidson, Near-field investigation of turbulence produced by multi-scale grids, Phys. Fluids **24**, 035103 (2012).
[8] M. Gad-El-Hak and S. Corrsin, Measurements of the nearly isotropic turbulence behind a uniform jet grid, J. Fluid Mech. **62**, 115 (1974).
[9] G. K. Batchelor, *The Theory of Homogeneous Turbulence* (Cambridge University Press, New York, 1953).
[10] G. Comte-Bellot and S. Corrsin, The use of a contraction to improve the isotropy of grid-generated turbulence, J. Fluid Mech. **25**, 657 (1966).
[11] L. Mydlarski and Z. Warhaft, On the onset of high-Reynolds-number grid-generated wind tunnel turbulence, J. Fluid Mech. **320**, 331 (1996).
[12] M. Hideharu, Realization of a large-scale turbulence field in a small wind tunnel, Fluid Dyn. Res. **8**, 53 (1991).
[13] H. Makita and K. Sassa, Active turbulence generation in a laboratory wind tunnel, in *Advances in Turbulence 3* (Springer, Berlin, Heidelberg, 1991), pp. 497-505.
[14] H. S. Kang, S. Chester, and C. Meneveau, Decaying turbulence in an active-grid-generated flow and comparisons with large-eddy simulation, J. Fluid Mech. **480**, 129 (2003).
[15] A. Thormann and C. Meneveau, Decay of homogeneous, nearly isotropic turbulence behind active fractal grids, Phys. Fluids **26**, 025112 (2014).
[16] E. Bodenschatz, G. P. Bewley, H. Nobach, M. Sinhuber, and H. Xu, Variable density turbulence tunnel facility, Rev. Sci. Instrum. **85**, 093908 (2014).
[17] G. I. Taylor, Statistical theory of turbulence-ii, Proc. R. Soc. Lond., A-Math. Phys. Sci. **151**, 444 (1935).
[18] T. V. Karman, The fundamentals of the statistical theory of turbulence, J. Aeronaut. Sci. **4**, 131 (1937).
[19] G. Birkhoff, Fourier synthesis of homogeneous turbulence, Commun. Pure Appl. Math. **7**, 19 (1954).
[20] P. Saffman, The large-scale structure of homogeneous turbulence, J. Fluid Mech. **27**, 581 (1967).
[21] E. van Doorn, C. M. White, and K. Sreenivasan, The decay of grid turbulence in polymer and surfactant solutions, Phys. Fluids **11**, 2387 (1999).
[22] M. R. Smith, R. J. Donnelly, N. Goldenfeld, and W. F. Vinen, Decay of Vorticity in Homogeneous Turbulence, Phys. Rev. Lett. **71**, 2583 (1993).
[23] S. R. Stalp, L. Skrbek, and R. J. Donnelly, Decay of Grid Turbulence in a Finite Channel, Phys. Rev. Lett. **82**, 4831 (1999).
[24] G. Comte-Bellot and S. Corrsin, Simple Eulerian time correlation of full-and narrow-band velocity signals in grid-generated, isotropicturbulence, J. Fluid Mech. **48**, 273 (1971).
[25] D. Hurst and J. Vassilicos, Scalings and decay of fractal-generated turbulence, Phys. Fluids **19**, 035103 (2007).
[26] N. Mazellier and J. Vassilicos, Turbulence without Richardson–Kolmogorov cascade, Phys. Fluids **22**, 075101 (2010).
[27] P. Valente and J. C. Vassilicos, The decay of turbulence generated by a class of multiscale grids, J. Fluid Mech. **687**, 300 (2011).
[28] P.-Å. Krogstad and P. Davidson, Freely decaying, homogeneous turbulence generated by multi-scale grids, J. Fluid Mech. **680**, 417 (2011).
[29] R. Poorte and A. Biesheuvel, Experiments on the motion of gas bubbles in turbulence generated by an active grid, J. Fluid Mech. **461**, 127 (2002).
[30] E. A. Variano and E. A. Cowen, A random-jet-stirred turbulence tank, J. Fluid Mech. **604**, 1 (2008).
[31] A. Pérez-Alvarado, L. Mydlarski, and S. Gaskin, Effect of the driving algorithm on the turbulence generated by a random jet array, Exp. Fluids **57**, 20 (2016).
[32] B. A. Johnson and E. A. Cowen, Turbulent boundary layers absent mean shear, J. Fluid Mech. **835**, 217 (2018).

[33] A. U. M. Masuk, A. Salibindla, S. Tan, and R. Ni, V-ONSET (vertical octagonal noncorrosive stirred energetic turbulence): A vertical water tunnel with a large energy dissipation rate to study bubble/droplet deformation and breakup in strong turbulence, Rev. Sci. Instrum. **90**, 085105 (2019).
[34] S. Tan, A. Salibindla, A. U. M. Masuk, and R. Ni, An open-source shake-the-box method and its performance evaluation, in *13th International Symposium on Particle Image Velocimetry — ISPIV 2019 Munich* (Germany, 2019).
[35] S. Tan, A. Salibindla, A. U. M. Masuk, and R. Ni, Introducing openLPT: New method of removing ghost particles and high-concentration particle shadow tracking, Exp. Fluids **61**, 1 (2020).
[36] E. A. Variano, E. Bodenschatz, and E. A. Cowen, A random synthetic jet array driven turbulence tank, Exp. Fluids **37**, 613 (2004).
[37] G. Bellani and E. A. Variano, Homogeneity and isotropy in a laboratory turbulent flow, Exp. Fluids **55**, 1 (2014).
[38] D. Carter, A. Petersen, O. Amili, and F. Coletti, Generating and controlling homogeneous air turbulence using random jet arrays, Exp. Fluids **57**, 1 (2016).
[39] S. Ghahremanian and B. Moshfegh, Investigation in the near-field of a row of interacting jets, J. Fluids Eng. **137**, 121202 (2015).
[40] K. Svensson, P. Rohdin, and B. Moshfegh, A computational parametric study on the development of confluent round jet arrays, Eur. J. Mech. - B/Fluids **53**, 129 (2015).
[41] K. Svensson, P. Rohdin, and B. Moshfegh, On the influence of array size and jet spacing on jet interactions and confluence in round jet arrays, J. Fluids Eng. **138**, 081206 (2016).
[42] M. Boussoufi, A. Sabeur-Bendehina, A. Ouadha, S. Morsli, and M. El Ganaoui, Numerical analysis of single and multiple jets, Eur. Phys. J.: Appl. Phys. **78**, 34814 (2017).
[43] B. T. Kannan and N. R. Panchapakesan, Influence of nozzle configuration on the flow field of multiple jets, Proc. Inst. Mech. Eng., Part G **232**, 1639 (2018).
[44] S. Ghahremanian, K. Svensson, M. J. Tummers, and B. Moshfegh, Near-field mixing of jets issuing from an array of round nozzles, Int. J. Heat Fluid Flow **47**, 84 (2014).
[45] M. Bisoi, M. K. Das, S. Roy, and D. K. Patel, Turbulent statistics in flow field due to interaction of two plane parallel jets, Phys. Fluids **29**, 125108 (2017).
[46] H. Teramoto and T. Kiwata, Flow characteristics of multiple round jets issuing from in-line nozzle arrangement, in *Symposium on Fluid-Structure-Sound Interactions and Control* (Springer, Singapore, 2017), p. 161.
[47] G. K. Jankee and B. Ganapathisubramani, Interaction and vectoring of parallel rectangular twin jets in a turbulent boundary layer, Phys. Rev. Fluids **6**, 044701 (2021).
[48] T. Berk, G. Gomit, and B. Ganapathisubramani, Vectoring of parallel synthetic jets: A parametric study, J. Fluid Mech. **804**, 467 (2016).
[49] H. J. Hussein, S. P. Capp, and W. K. George, Velocity measurements in a high-Reynolds-number, momentum-conserving, axisymmetric, turbulent jet, J. Fluid Mech. **258**, 31 (1994).
[50] S. B. Pope and S. B. Pope, *Turbulent Flows* (Cambridge University Press, Cambridge, 2000).
[51] P. C. Chu, J. H. Lee, and V. H. Chu, Spreading of turbulent round jet in coflow, J. Hydraul. Eng. **125**, 193 (1999).
[52] A. N. Kolmogorov, The local structure of turbulence in incompressible viscous fluid for very large Reynolds numbers, Proc. R. Soc. Lond., A: Math. Phys. Sci. **434**, 9 (1991).
[53] R. Ni, K.-Q. Xia, Kolmogorov constants for the second-order structure function and the energy spectrum, Phys. Rev. E **87**, 023002 (2013).
[54] K. R. Sreenivasan, An update on the energy dissipation rate in isotropic turbulence, Phys. Fluids **10**, 528 (1998).
[55] W. K. George, The decay of homogeneous isotropic turbulence, Phys. Fluids A **4**, 1492 (1992).
[56] C. Or, K. M. Lam, and P. Liu, Potential core lengths of round jets in stagnant and moving environments, J. Hydro-Environ. Res. **5**, 81 (2011).